Stability Analysis of Grid-Following and Grid-Forming Converters Based on State-Space Modelling

Gao, Xian; Zhou, Dao; Anvari-Moghaddam, Amjad; Blaabjerg, Frede

Published in:
I E E E Transactions on Industry Applications

DOI (link to publication from Publisher):
10.1109/TIA.2024.3353158

Publication date:
2024

Document Version
Accepted author manuscript, peer reviewed version

Citation for published version (APA):
Gao, X., Zhou, D., Anvari-Moghaddam, A., & Blaabjerg, F. (2024). Stability Analysis of Grid-Following and Grid-Forming Converters Based on State-Space Modelling. *I E E E Transactions on Industry Applications*, *60*(3), 4910-4920. https://doi.org/10.1109/TIA.2024.3353158

Stability Analysis of Grid-Following and Grid-Forming Converters Based on State-Space Modelling

Xian Gao, *Student Member, IEEE,* Dao Zhou, *Senior Member, IEEE,* Amjad Anvari-Moghaddam, *Senior Member, IEEE,*
and Frede Blaabjerg, *Fellow, IEEE*

AAU Energy, Aalborg University, Aalborg, Denmark
xiga@energy.aau.dk; zda@energy.aau.dk; aam@energy.aau.dk; fbl@energy.aau.dk

***Abstract* - This paper conducts a comprehensive analysis and comparison of the control loops of the grid-following and grid-forming voltage source converters connected to the power grid. Eigenvalue trajectories are studied in order to obtain an accurate stability analysis. A time-domain simulation model of a 1.5 kW grid-connected converter is developed by using Matlab/Simulink to investigate the stability of the grid-following and grid-forming control under different short-circuit ratios. The stability boundaries of the grid-following control and the grid-forming control are explored and compared with theoretical analysis. The result reveals that the grid-following control is better suited for a stiff power grid, while the grid-forming control is more suitable for a weak power grid. Finally, an experimental prototype is established to verify the effectiveness of the theoretical analysis.**

***Index Terms*— Grid-following converter, grid-forming converter, state-space model, stability boundaries.**

I. INTRODUCTION

Facing the threats of fossil resource depletion and ecological environment deterioration, renewable energy sources (RESs) to be integrated into the power system have drawn more and more attention in recent years. Moreover, with the continuous declining cost of RESs generation, the primary energy in the power grid will mainly be generated from RESs in the future.

The RESs are normally connected to the power grid through grid-connected converters using grid-following (GFL) control, which has a fast response but provides almost no inertia for the power grid to perform the frequency control [1]. With the increasing penetration of RESs, many large synchronous generators will be phasing out, so the spinning reserve capacity will be reduced as well as the inertia and damping of the power grid. In order to solve the stability challenges for the power grid, grid-forming (GFM) control strategies have been emerging. One of the most popular GFM control strategies is the virtual synchronous generator (VSG) control, which enables the converter to mimic the characteristics of synchronous generators to provide inertia and damping for the power grid.

However, both the GFL control and the GFM control have small-signal instability problems [2]. It is noted that the short-circuit ratio (SCR) is usually defined to measure the strength of the power grid. According to the IEEE Standard 1204-1997 [3], when the SCR is less than 2, the power grid is very weak. Alternatively, when the SCR is larger than 3, the power grid is considered as strong. The GFL control loses stability in a weak power grid because of the asymmetric positive feedback mechanism introduced by the phase-locked loop (PLL) structure [4], [5]. On the contrary, the GFM control loses stability in a stiff power grid, since little phase difference between the converter and grid voltages may lead to large active power fluctuations [6]. Actually, numerous papers have investigated the stability of GFL and GFM converters connected to power grids with different SCRs [7]. However, to some extent, they just tested the power transfer ability of GFL and GFM converters and compared the maximum power that can be transferred under power grids with different SCRs. A comprehensive and fair comparison is needed to be conducted to evaluate the performances of GFL and GFM converters under the power grids with diverse SCRs, while upholding the constant output power.

The stability assessment of a power system incorporates various established techniques, including the state-space model and impedance model [8], [9]. The eigenvalue analysis method, which relies on the linearized state-space model of the system in its steady-state operation, enables precise evaluations. This method involves the construction of a state-space model and the examination of eigenvalue distribution on a complex plane to facilitate assessments of stability. For the impedance model, it divides the system into smaller, independent subsystems and employs the Nyquist stability criterion to ascertain the stability of the impedance ratio between the grid and converter. Moreover, modifications in one subsystem's parameters do not impact other subsystems, obviating the need for the reconstruction of the entire system model. Consequently, this approach allows for convenient model updates in the event of changes to subsystem parameters. In this paper, the eigenvalue analysis method is selected by using the state-space model to ensure accurate stability analysis.

To study the aforementioned issues and obtain an accurate result, the stability analysis of the GFL converter and the GFM converter based on the state-space model is presented in this paper [10]. The main contributions of this work can be summarized as follows. 1) The control loops of the GFL converter and the GFM converter are established in details. 2) The full-order state-space models of the GFL converter and the GFM converter are presented, and their eigenvalue trajectories are used for detailed stability analysis. 3) The stability boundaries of the GFL control and the GFM control are obtained by changing the SCR continuously. 4) Comparative analysis is executed to assess the differences existing among the stability boundaries derived from theoretical analysis, simulations, and experiments.

The remaining part of the paper is organized as follows. Section II illustrates the control loops of the GFL converter and the GFM converter, respectively. In Section III, the eigenvalue trajectories are drawn to compare the stability of the GFL converter and GFM converter. In Section IV, a time-domain simulation model is built in Matlab/Simulink to verify the theoretical stability analysis. In Section V, experimental validations are presented. Finally, concluding remarks are drawn in Section VI.

II. SYSTEM MODELING

The configuration of a three-phase grid-connected system is shown in Fig. 1. L_f and C_f are the output filter inductor and capacitor, respectively; Z_g is the grid impedance; u_{dc} is the dc-link voltage; u_a, u_b and u_c are the converter output voltages; u_{pcca}, u_{pccb} and u_{pccc} are the voltages at the point of common coupling (PCC); i_a, i_b and i_c are the converter currents; i_{ga}, i_{gb} and i_{gc} are the grid currents; i_{Ca}, i_{Cb} and i_{Cc} are the capacitor currents.

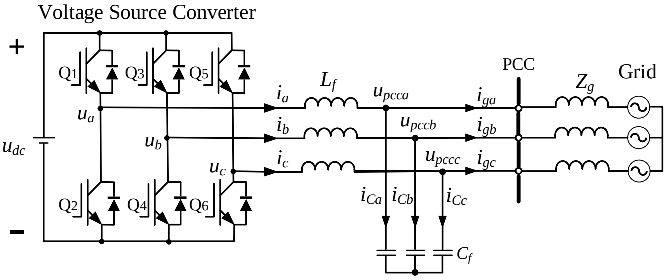

Fig. 1. Configuration of a three-phase converter connected to the power grid.

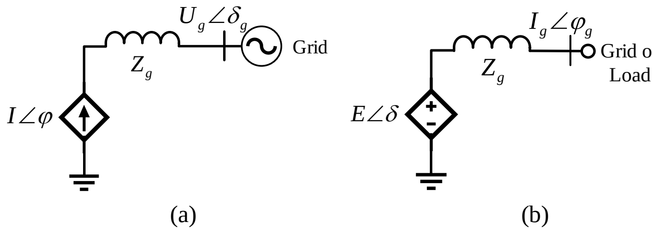

(a) (b)

Fig. 2. Simplified representation of power converters. (a) Grid-following (GFL) converter; (b) Grid-forming (GFM) converter.

The power converters can be controlled as GFL converters and GFM converters. The behavior of the GFL converter is similar to that of the controlled current source, while the behavior of the GFM converter is similar to that of the controlled voltage source. The simplified representations of the power converters are shown in Fig. 2.

A. Grid-following converter

The GFL converter is widely applied in distributed RES-based power grids and it is typically using a PLL to synchronize with the grid. In the outer control loop, the active and reactive power can be controlled directly through PQ controllers or indirectly through dc-link voltage and PCC voltage regulation [11]. The type of outer loop is determined by the applications, e.g., in a grid-connected photovoltaic system, a DC-DC converter will be employed to optimize the power extraction and it will alter the control objectives of the outer loop. Nevertheless, the current control is always selected as the inner loop to regulate the current injected into the power grid [12], [13]. The reference of the current control loop is set by the outer control loop. Notably, a PLL unit is used for the reference frame transformation to keep the power converter synchronized with the power grid in all cases.

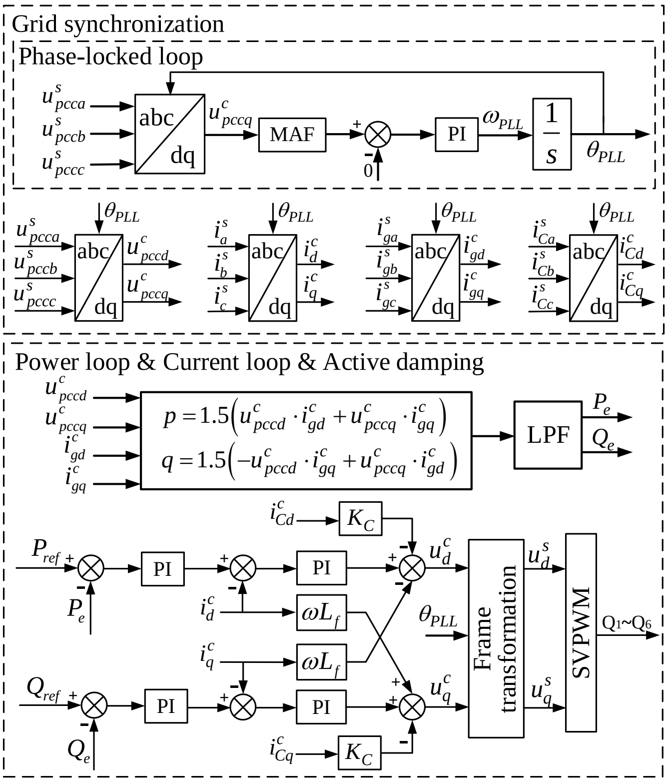

Fig. 3. Control scheme of the grid-following (GFL) converter.

Outer power control is adopted in this paper. To simplify the analysis, the dc side is represented as an ideal dc voltage source. The control scheme of the GFL converter is shown in Fig. 3. The control scheme mainly consists of three parts, including the PLL unit, power control loop, and current control loop [14]. P_{ref} and Q_{ref} are the references of the active and reactive power, respectively; P_e and Q_e are the output active and reactive power; K_C is the proportional coefficient of the capacitor current feedback. Subscripts *d* and *q* denote the d-axis and q-axis components of a variable, respectively.

The PLL unit plays an important role in the control of the grid-tied converter. In order to obtain a good performance, a moving average filter (MAF) based PLL is adopted [15]. It enables the converter to synchronize with the power grid. When the system is in a steady state, the PLL can track the phase angle of the PCC voltage accurately. In the case that small-signal disturbances are added to the PCC voltage, there is a small difference θ_{PLL}-θ_s between the control synchronizing frame, which is determined by the PLL unit, and the actual system synchronizing frame, which is defined by the PCC voltage [16], [17]. The relationship between two synchronizing frames is shown in Fig. 4.

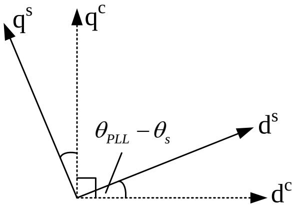

Fig. 4. The actual system synchronizing frame and control synchronizing frame.

The actual system synchronizing frame can be transformed into the control synchronizing frame through a rotating matrix T_θ. The matrix T_θ can be given as:

$$T_\theta = \begin{bmatrix} \cos(\theta_{PLL}-\theta_s) & \sin(\theta_{PLL}-\theta_s) \\ -\sin(\theta_{PLL}-\theta_s) & \cos(\theta_{PLL}-\theta_s) \end{bmatrix} \approx \begin{bmatrix} 1 & \theta_{PLL}-\theta_s \\ \theta_s-\theta_{PLL} & 1 \end{bmatrix} \quad (1)$$

The transformations between the actual system synchronizing frame and the control synchronizing frame can be given as [18], [19]:

$$\begin{bmatrix} x_d^c \\ x_q^c \end{bmatrix} = T_{\Delta\theta} \begin{bmatrix} x_d^s \\ x_q^s \end{bmatrix} \approx \begin{bmatrix} 1 & \theta_{PLL}-\theta_s \\ \theta_s-\theta_{PLL} & 1 \end{bmatrix} \begin{bmatrix} x_d^s \\ x_q^s \end{bmatrix} \quad (2)$$

where the variable *x* represents the converter current, the grid current, the PCC voltage and the output voltage. The variables in the actual system synchronizing frame are marked with superscript *s*, while the variables in the control synchronizing frame are marked with superscript *c*.

If small-signal perturbations are applied to (2) and the steady-state values are neglected, the linearized small-signal model of transformations can be given as:

$$\begin{bmatrix} \Delta x_d^c \\ \Delta x_q^c \end{bmatrix} = \begin{bmatrix} \Delta x_d^s \\ \Delta x_q^s \end{bmatrix} + \begin{bmatrix} X_{q0} \\ -X_{d0} \end{bmatrix} \cdot \Delta\theta \quad (3)$$

where the prefix *Δ* denotes the small disturbance of variables, the subscript *0* denotes the steady-state values.

By using the PCC voltage orientation, active power and reactive power of the converter can be regulated by d-axis and q-axis converter currents. Consequently, the output of the power control loop serves as the reference for the inner current control loop.

The inner current controller is adopted to regulate the converter current to follow the reference set by the outer voltage loop. The output voltage reference of the converter is obtained from the inverse Clark and Park transformation of the current controller output [11]. The voltage reference is then used for the space vector pulse-width modulation (SVPWM). It is worth mentioning that an active damping method is adopted to suppress the resonances of the LC filter without sacrificing the efficiency of the converter [20], [21]. As shown in Fig. 3, the capacitor current i_{Cd}, i_{Cq} is feedbacked through a proportional unit K_C in the current control loop.

B. Grid-forming converter

With the increasing penetration of RESs, the inertia of the power grid will decrease since many large synchronous generators are phasing out. In order to solve the stability problems for the power electronic-based power systems, GFM control strategies have been emerging.

The VSG control is adopted in this paper, and the control scheme of the GFM converter is shown in Fig. 5. The control scheme is mainly composed of three parts, including the VSG algorithm loop, voltage control loop and current control loop. *J* is the emulated moment of inertia; *D* is the damping

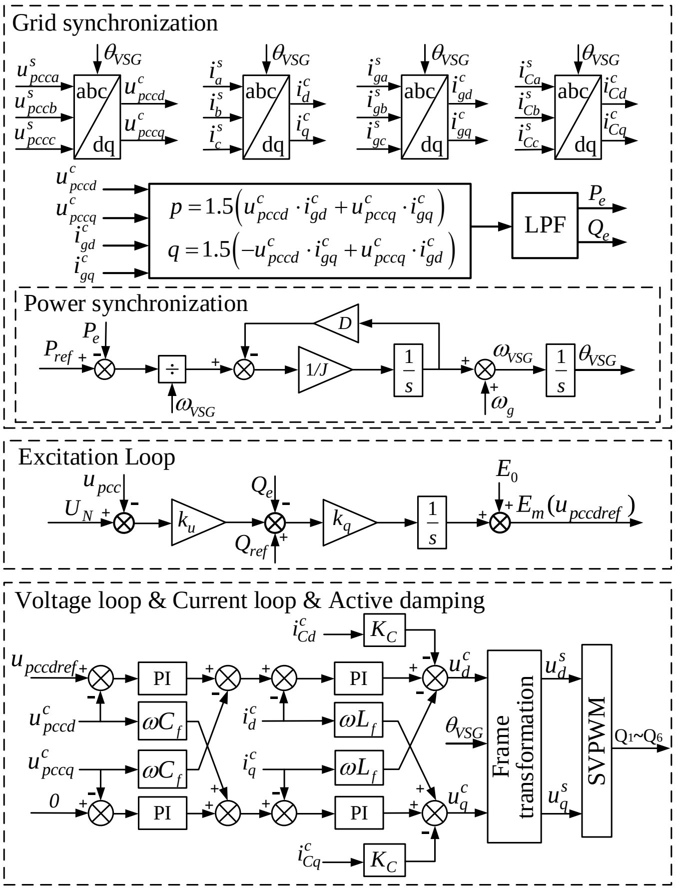

Fig. 5. Control scheme of the grid-forming (GFM) converter.

coefficient; k_q is the integrity coefficient; k_u is the voltage droop coefficient; ω_g is the rated grid frequency; E_m and θ_{VSG} are the amplitude and phase angle of the reference voltage; E_0 is the no-load electromotive force of the converter; U_N is the peak value of the rated grid voltage.

The VSG algorithm is mainly composed of a power-frequency controller and an excitation controller, which can be given as:

$$\begin{cases} J\dfrac{d\omega_{VSG}}{dt} = \dfrac{P_{ref}}{\omega_{VSG}} - \dfrac{P_e}{\omega_{VSG}} - D\left(\omega_{VSG} - \omega_g\right) \\ \dfrac{d\theta_{VSG}}{dt} = \omega_{VSG} \end{cases} \tag{4}$$

$$E_m = E_0 + k_q \int \left(k_u\left(U_N - u_{pcc}\right) + Q_{ref} - Q_e\right) \tag{5}$$

The voltage control loop is adopted to regulate the PCC voltage to follow the reference set by the VSG algorithm loop. The difference between the actual system synchronizing frame and the control synchronizing frame is caused by the phase angle generated from the power synchronization unit. In addition, the current control of the GFM converter is the same as that of the GFL converter as aforementioned.

III. STABILITY ANALYSIS BASED ON STATE-SPACE MODEL

To compare the performances of grid-connected converters under different SCRs, state-space models of the whole system are built based on the small-signal models. The state-space expression of GFL and GFM converters can be given as:

$$\Delta \dot{x}_{sys\_GFL} = A_{sys\_GFL}\Delta x_{sys\_GFL} + B\begin{bmatrix}\Delta u_{gd}^{s} \\ \Delta u_{gq}^{s}\end{bmatrix} \tag{6}$$

$$\Delta \dot{x}_{sys\_GFM} = A_{sys\_GFM}\Delta x_{sys\_GFM} + B\begin{bmatrix}\Delta u_{gd}^{s} \\ \Delta u_{gq}^{s}\end{bmatrix} \tag{7}$$

where $\Delta x_{sys\_GFL}=[\Delta x_{PLL}, \Delta x_{cal}, \Delta x_{PQ}, \Delta x_c, \Delta x_{LCL}]^T$, $\Delta x_{sys\_GFM}=[\Delta x_{VSG}, \Delta x_{cal}, \Delta x_u, \Delta x_c, \Delta x_{LCL}]^T$, A_{sys_GFL}, A_{sys_GFM}, and B are shown in Appendix.

A case study of a 1.5 kW grid-connected converter is built and its key parameters are listed in TABLE I [22]. According to the parameters and state-space matrix A_{sys_GFL}, A_{sys_GFM}, the eigenvalue trajectories are drawn to compare the stability of the GFL and GFM converters under different SCRs [23]. The initial SCR is chosen as 5.21 with the L_g is 3 mH and R_g is 0.18 Ω. The ratio between L_g to R_g remains constant. In order to get accurate results, the intervals of the change of the values of the L_g and R_g are set as 20 μH and 1.4 mΩ, respectively.

TABLE I

PARAMETERS OF 1.5 KW GRID-CONNECTED CONVERTER.

Grid Parameters		
u_g	Grid RMS voltage	50 V
f_g	Grid frequency	50 Hz
L_g	Grid inductance	0.5-15.5 mH
R_g	Grid resistance	0.03-0.93 Ω
ω_g	Grid angular frequency	314 rad/s
Converter Parameters		
u_{dc}	DC-side voltage	600 V
L_f	Filter inductance	3 mH
C_f	Filter capacitance	20 μF
P_{ref}	Rated active power	1.5 kW
f_s	Switching frequency	10 kHz
f_{sa}	Sampling frequency	20 kHz
Control Parameters for grid-following converter		
ω_{pll}	Bandwidth of phase-locked loop	13.4 rad/s
ω_{PQ}	Bandwidth of power loop	110 rad/s
ω_i	Bandwidth of current loop	1030 rad/s
K_C	Proportional gain of capacitor current feedback	1
ω_c	Cut-off frequency of LPF	100 rad/s
Control Parameters for grid-forming converter		
ω_{vsg}	Bandwidth of VSG loop	2.77 rad/s
ω_u	Bandwidth of voltage loop	23.4 rad/s
ω_i	Bandwidth of current loop	1030 rad/s
K_C	Proportional gain of capacitor current feedback	1
ω_c	Cut-off frequency of LPF	100 rad/s
D	Damping coefficient	9
J	Virtual inertia	0.2 kg/m^2
k_u	Q-U loop coefficient	30
k_q	Integrity coefficient	0.01
E_0	No-load electromotive force of the converter	70.7 V
U_N	Peak value of the rated grid voltage	70.7 V
Q_{ref}	Rated reactive power	0 kVar

When the SCR decreases from 5.21 to 1.58, the eigenvalue trajectories of the GFL converter is plotted in Fig. 6. When the SCR decreases from 5.21 to 1.00, the eigenvalue trajectories of the GFM converter is plotted in Fig. 7. When the SCR is less than 1.58, the eigenvalue λ_1 of the GFL converter moves towards the right half plane, which means the system becomes unstable. However, all the eigenvalues of the GFM converter are still in the left half plane, indicating a stable system.

When the SCR increases from 5.21 to 31.26, the eigenvalue trajectories of the GFL converter is plotted in Fig. 8. When the SCR increases from 5.21 to 12.02, the eigenvalue trajectories of the GFM converter is plotted in Fig. 9. All the eigenvalues of the GFL converter stay in the left half plane with SCR changing from 5.21 to 31.26. Compared to the GFL converter, when the SCR is larger than 11.67, the eigenvalues λ_1 and λ_2 of the GFM converter move into the right half plane, and the system may lose stability, which is opposite to the condition when the SCR decreases.

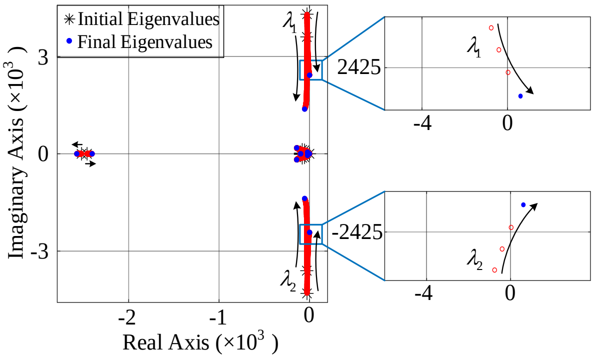

Fig. 6. Eigenvalue trajectories of the grid-following (GFL) converter in the case that the SCR is changed from 5.21 (Initial) to 1.58 (Final).

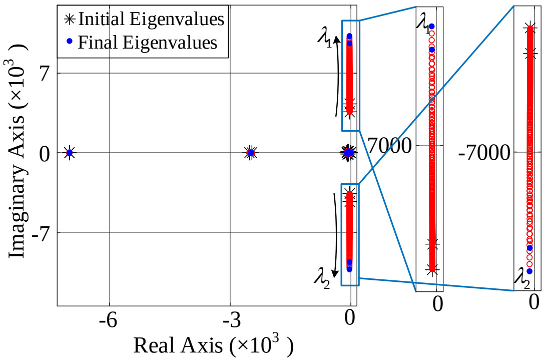

Fig. 7. Eigenvalue trajectories of the grid-forming (GFM) converter in the case that the SCR is changed from 5.21 (Initial) to 1.00 (Final).

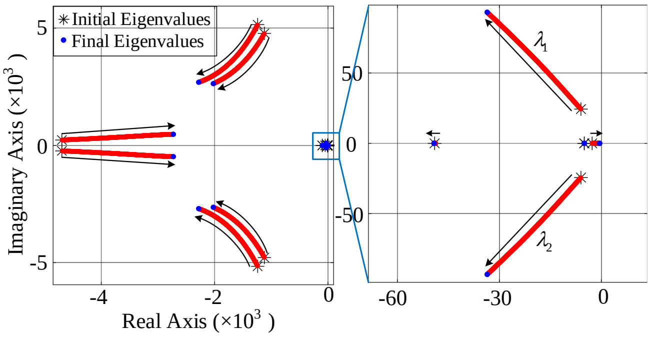

Fig. 8. Eigenvalue trajectories of the grid-following (GFL) converter in the case that the SCR is changed from 5.21 (Initial) to 31.26 (Final).

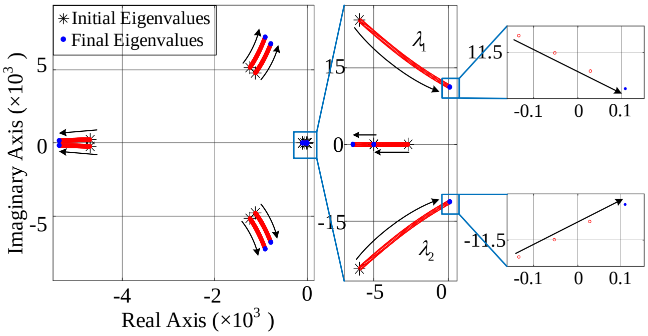

Fig. 9. Eigenvalue trajectories of the grid-forming (GFM) converter in the case that the SCR is changed from 5.21 (Initial) to 12.02 (Final).

IV. SIMULATION RESULTS

In order to verify the aforementioned stability analysis, the case study system is established in Matlab/Simulink to investigate the various control schemes. The parameters are the same as those specified in TABLE I.

As shown in Fig. 10 and Fig. 11, when the SCR decreases, the simulation results are presented for variable SCRs. In the case that the SCR is changed from 5.21 to 1.57, the voltages at the PCC and the converter output currents, the reference and feedback of the output active power, the reactive power, the PCC voltage, current control loop, and the frequency of the GFL converter are shown in Fig. 10. Similarly, in the case that the SCR is changed from 5.21 to 1.00, the voltages at the PCC

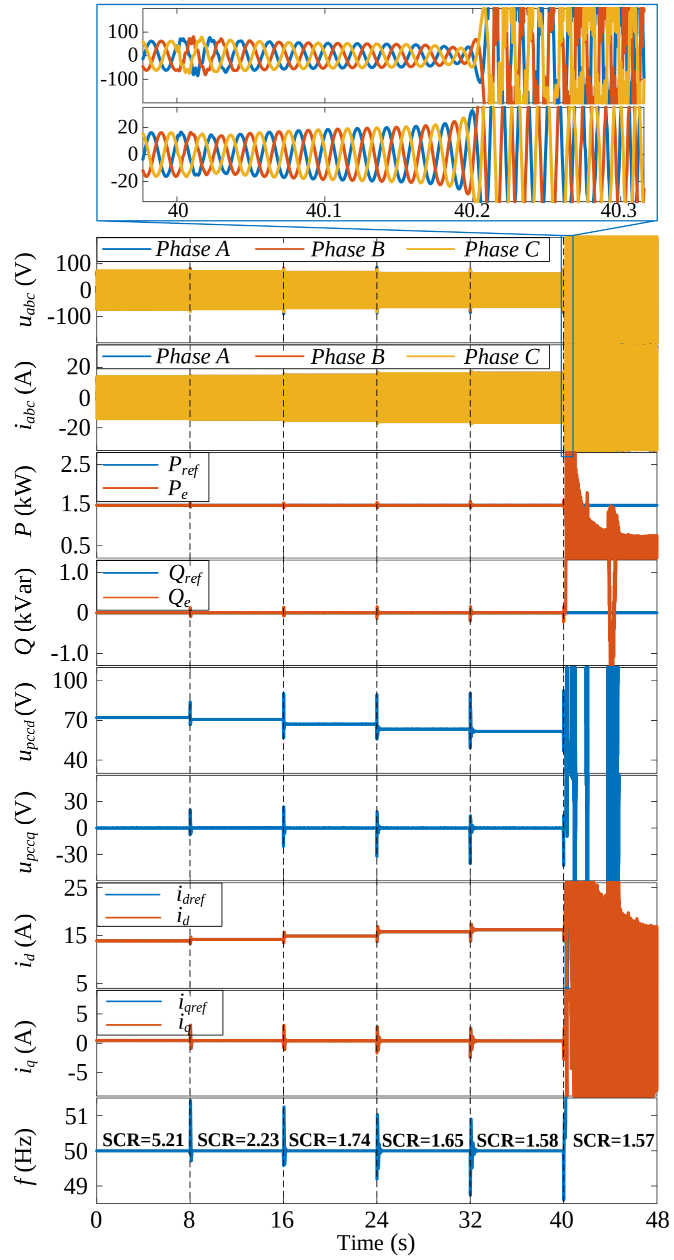

Fig. 10. Simulation results of the grid-following (GFL) converter when the SCR is changed from 5.21 to 1.57.

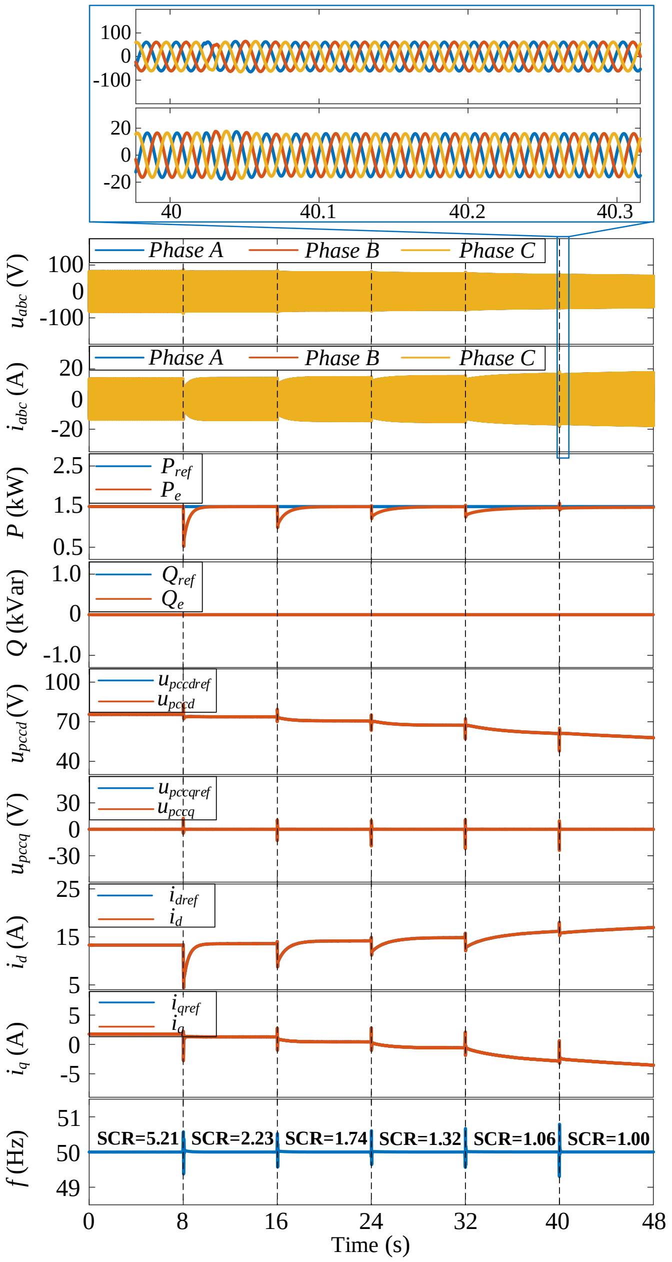

Fig. 11. Simulation results of the grid-forming (GFM) converter when the SCR is changed from 5.21 to 1.00.

and the converter output currents, the reference and feedback of VSG algorithm loop, voltage control loop, current control loop, and the frequency of GFM converter are shown in Fig. 11.

The power flow is defined as from the converter to the power grid. If the value of SCR decreases, the corresponding inductance and resistance of the grid impedance increase, which lead to higher power losses over the transmission line. The converter needs to provide more active power to keep the active power injected into the power grid constant. As a result, the d-axis component of the converter output current increases [24]. Because the GFL control keeps the output power constant, the PCC voltages will decrease accordingly, which is shown in Fig. 10. However, there is a droop relationship between the reactive power and the voltages at the PCC under the GFM control, the reactive power will increase in order to support the voltage back to normal, which is shown in Fig. 11.

Moreover, as shown in Fig. 11, it can be noted that the response of the system becomes slower when the SCR decreases. This is because when the SCR decreases, the grid impedances will increase, which may lead to a slower response.

When the SCR is below 1.58, the system with GFL control cannot remain stable. On the other hand, when the SCR is 1, the system with GFM control can still achieve stable

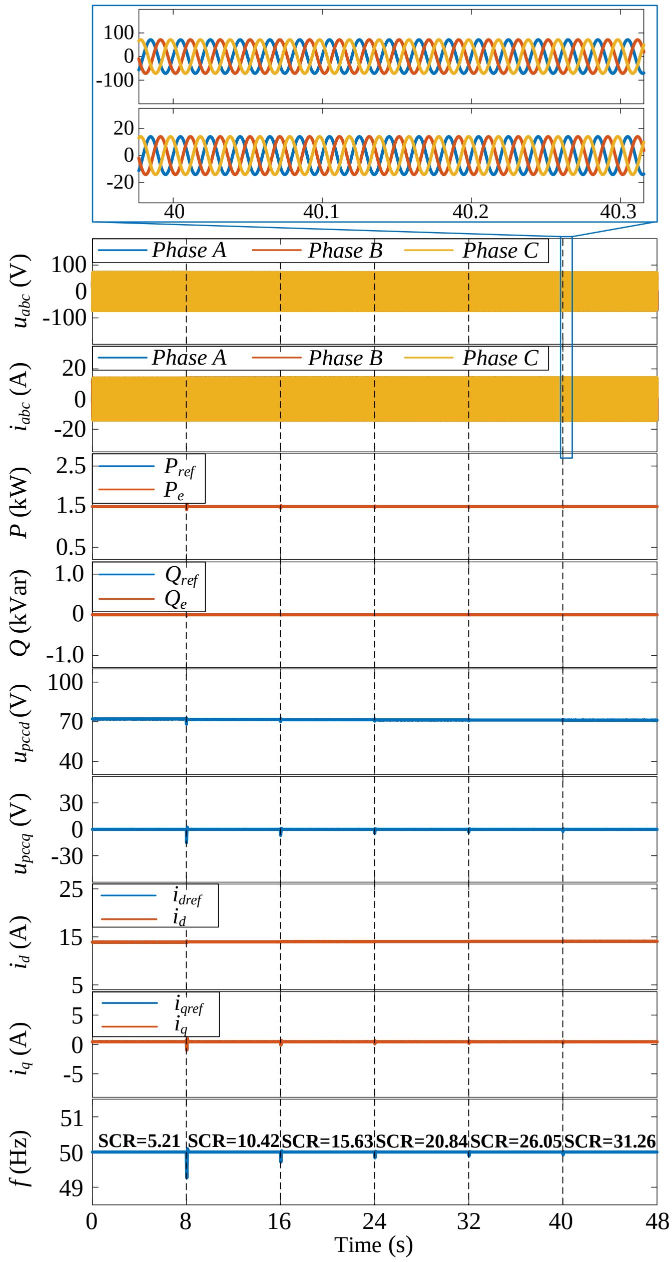

Fig. 12. Simulation results of the grid-following (GFL) converter with SCR changing from 5.21 to 31.26.

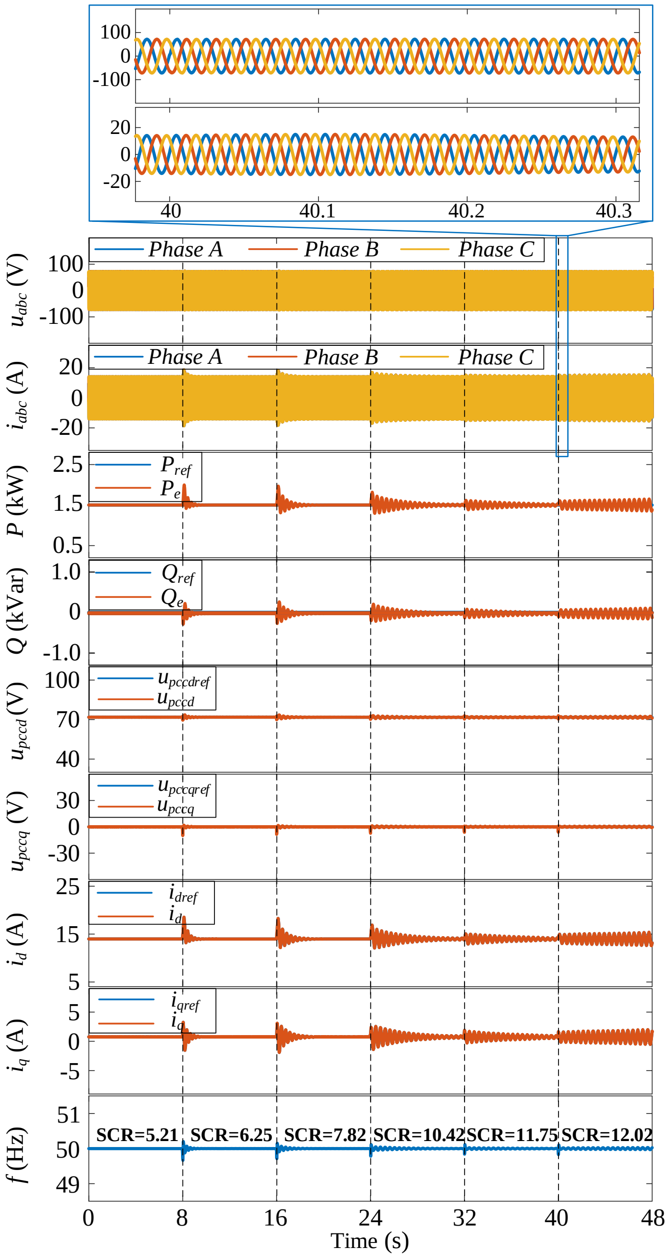

Fig. 13. Simulation results of the grid-forming (GFM) converter with SCR changing from 5.21 to 12.02.

operation. The GFM converter is therefore more suitable for weak power grid operation. Compared to the results from the theoretical analysis, both the stability boundary obtained from the state-space model and the stability boundary obtained from the simulation results are the same.

In the case that the grid condition becomes stronger, the simulation results with the GFL and GFM control are also studied. The voltages at the PCC and the converter output currents, the reference and feedback of the output active power, the reactive power, the PCC voltage, current control loop, and the frequency of the GFL with SCR changing from 5.21 to 31.26 are shown in Fig. 12. The voltages at the PCC and the converter output currents, the reference and feedback of the VSG algorithm loop, voltage control loop, current control loop, and the frequency of GFM converter with SCR changing from 5.21 to 12.02 are shown in Fig. 13.

When the SCR increases, the GFL converter stays stable while the GFM converter cannot maintain stability when the SCR is larger than 11.75. It can be seen that the GFL converter is more suitable for stiff power grid operation. The stability boundary of the GFM converter obtained from theoretical analysis is 11.67, which has a slight difference compared to the stability boundary obtained from simulation. The analysis based on the state-space model and the simulation about the influence of the SCR on the stability of the power grid is consistent. Moreover, the stability boundary obtained from these two ways are almost the same. The stability boundaries obtained from the theoretical analysis and the simulation are summarized in TABLE II.

TABLE II

COMPARISON OF STABILITY BOUNDARIES OBTAINED FROM THEORETICAL ANALYSIS AND SIMULATION.

Converter Type	Theoretical Analysis	Simulation Result
GFL	1.58	1.58
GFM	11.67	11.75

It is worth mentioning that if the value of SCR is already high enough, a little change of the inductance will lead to a large change of SCR. Thus, it is easier to get some differences between the theoretical analysis and simulation results under the stiff power grid compared with the weak power grid.

V. EXPERIMENTAL VALIDATION

As shown in Fig. 14, the experimental setup of a three-phase grid-connected system is established. The grid is simulated by a high-fidelity linear amplifier APS 15000 [25]. The applied grid-connected converter is an Imperix standard PEB-SiC module [26], and it is controlled by the B-BOX RCP control platform using the software ACG SDK. The B-BOX RCP prototyping controller can be programmed using

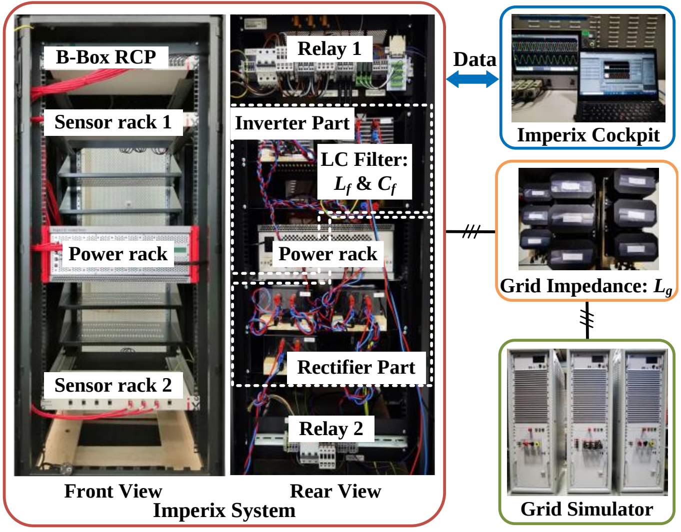

Fig. 14. The experimental setup of a grid-connected system.

simulation software through an automated code generation toolchain. The Imperix cockpit is used to monitor and regulate any control variable in real-time. The current and voltage sensing circuits are designed by using LEM LAH50-P and LEM LV20-P sensors, respectively.

It should be mentioned that for the startup process of the GFM converter, the possible oscillation of the active power results in bidirectional power flow between the power grid and the dc power supply. As the dc power supply cannot absorb the power, the power flow from the power grid to the dc side may induce a shutdown of the dc power supply. In order to overcome this problem and realize bidirectional power flow between the dc side and the power grid, a back-to-back three-phase converter is built in the experimental setup. However, since the dc voltage is established through the rectifier, the couplings from the dc-link voltage inevitably have some impacts on the inverter part. Nevertheless, these effects are independent of the inverter control, so the design and control of the rectifier will not be illustrated in details.

Moreover, it is worth mentioning that the different SCRs are achieved by changing the value of grid impedance which is kept the same test condition as that of simulations. In the experiment, in order to realize the continuous change of grid impedance and avoid startup from the power grids with different SCRs, four relays are used to realize the change of grid impedance. The parameters of the setup are the same as those specified in TABLE I.

When the SCR decreases from 5.21 to 1.74, the experimental waveforms of three-phase grid currents and the voltage of phase A of the GFL converter are shown in Fig. 15. Similarly, as shown in Fig. 16, the performance of the GFM converter is presented with the decreasing SCR.

For the GFL converter, when the SCR is 1.79, the waveforms of the current and voltage are severely distorted. When the SCR becomes 1.74, the system cannot stay stable. Both the current and voltage have large overshoots, which trigger the protection and lead to the shutdown of the converter. However, for the GFM converter, the system can still maintain a stable operation even when the SCR decreases to 1. The stability boundary obtained from the experiment is 1.79, while the stability boundary obtained from the simulation is 1.58. The reason for the difference between the simulation results and experimental waveforms lies in the resistance of the inductors and the impedance of the connection lines, which may increase the grid impedance and result in a decrease of the SCR.

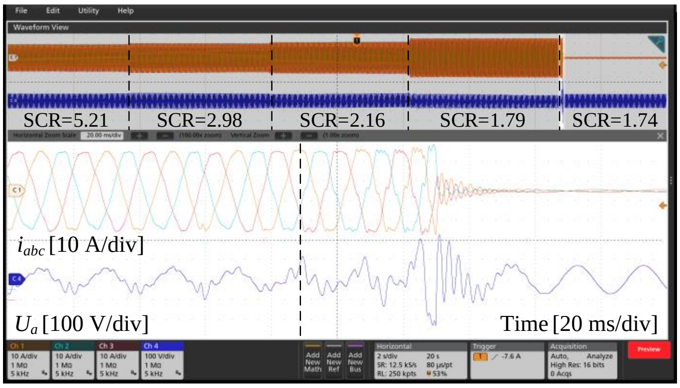

Fig. 15. Measured waveforms of the grid-following (GFL) converter with SCR changing from 5.21 to 1.74.

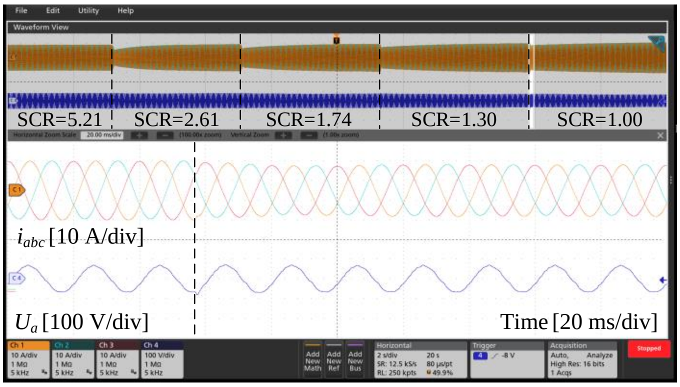

Fig. 16. Measured waveforms of the grid-forming (GFM) converter with SCR changing from 5.21 to 1.00.

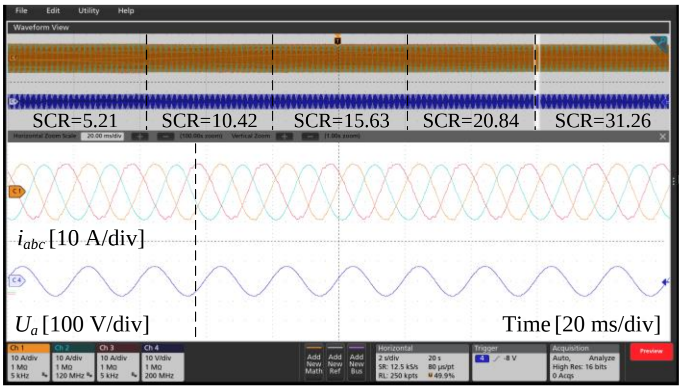

Fig. 17. Measured waveforms of the grid-following (GFL) converter with SCR changing from 5.21 to 31.26.

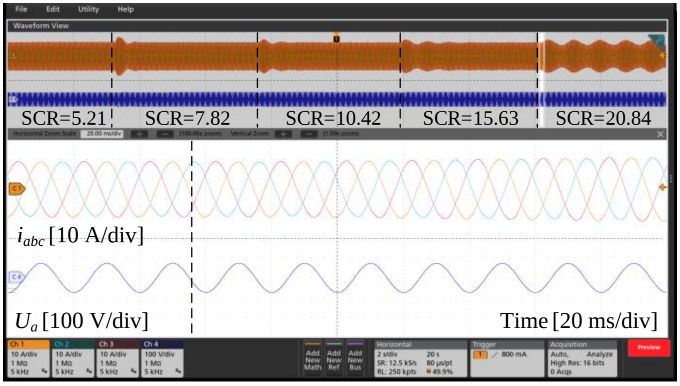

Fig. 18. Measured waveforms of the grid-forming (GFM) converter with SCR changing from 5.21 to 20.84.

Similarly, the three-phase grid currents and the voltage of phase A of the GFL converter are shown in Fig. 17, when the SCR increases from 5.21 to 31.26. As shown in Fig. 18, by using the GFM control, the grid currents and the grid voltage of phase A are presented when the SCR increases from 5.21 to 20.84.

When the SCR changes from 5.21 to 31.26, the GFL converter can always stay stable. When the SCR is 20.84, the GFM converter cannot maintain stability anymore, and it starts to oscillate until the protection is triggered and then the system shuts down. It can be seen that the GFL converter is more suitable for stiff power grid operation. The stability boundary obtained from the experiment is larger than the simulation. The reason is that the total real resistance of the grid impedance is larger than the simulation, which may lead to a decrease of the SCR. Furthermore, according to the literature [27] and [28], increasing the resistance can change the magnitude of the output impedance of the inverter at the low-frequency range to avoid instability risk. The determinants of the impedance ratio matrix are also drawn, which shows that the increase of resistance makes the poles move towards the left half plane. It is worthwhile to note that little change of the inductance will lead to a large change of SCR, if the value of SCR is already high enough. However, it is very difficult to fine-tune the SCR because the value of the existing inductors in the laboratory is not small enough.

VI. CONCLUSION

This paper has analyzed the control loops of the GFL converter and the GFM converter in details. The results from the stability analysis based on the state-space model were consistent with that of time-domain simulations. The GFL converter encountered some instability in the power grid with a low SCR, while the GFM converter suffered from instability in the power grid with a high SCR. Moreover, the stability boundaries of the GFL converter and the GFM converter are obtained. It has indicated that the GFL converter could be more suitable for the stiff power grid while the GFM converter is more suitable for the weak power grid. The theoretical analysis and simulation yield nearly identical stability boundaries. However, minor inductance changes significantly affect the SCR which leads to some differences especially under the stiff power grid. The differences between the simulation and experiment results are caused by inductor resistance, connection line impedance, and challenges in fine-tuning the SCR due to limited inductor values in the laboratory.

APPENDIX

$$A_{sys\_GFL}=\begin{bmatrix} A_{PLL} & [0]_{3\times2} & [0]_{3\times2} & [0]_{3\times2} & B_{PLL} \\ [0]_{2\times3} & A_{cal} & [0]_{2\times2} & [0]_{2\times2} & B_{cal} \\ [0]_{2\times3} & B_{PQ} & A_{PQ} & [0]_{2\times2} & [0]_{2\times6} \\ B_{c1} & B_{c3}D_{PQ} & B_{c3}C_{PQ} & A_c & B_{c2} \\ B_{LCL1}D_{c4} & B_{LCL1}D_{c1}D_{PQ} & B_{LCL1}D_{c1}C_{PQ} & B_{LCL1}C_c & B_{LCL1}D_{c2}+A_{LCL} \end{bmatrix} \tag{8}$$

$$A_{sys\_GFM}=\begin{bmatrix} A_{VSG} & B_{VSG1} & [0]_{3\times2} & [0]_{3\times2} & B_{VSG2} \\ [0]_{2\times3} & A_{cal} & [0]_{2\times2} & [0]_{2\times2} & B_{cal} \\ B_{u1} & [0]_{2\times2} & A_u & [0]_{2\times2} & B_{u2} \\ B_{c1}+B_{c3}D_{u1} & [0]_{2\times2} & B_{c3}C_u & A_c & B_{c2}+B_{c3}D_{u2} \\ B_{LCL1}(D_{c4}+D_{c1}D_{u1}) & [0]_{6\times2} & B_{LCL1}D_{c1}C_u & B_{LCL1}C_c & B_{LCL1}D_{c2}+B_{LCL1}D_{c1}D_{u2}+A_{LCL} \end{bmatrix} \tag{9}$$

$$B=\begin{bmatrix} [0]_{10\times2} \\ B_{LCL2} \end{bmatrix} \tag{10}$$

where E represents an identity matrix, $A_{cal}=-\omega_c E_{2\times2}$, $B_{PQ}=-E_{2\times2}$, $C_c=k_{ic}E_{2\times2}$, $D_{c1}=k_{pc}E_{2\times2}$, $C_u=k_{iu}E_{2\times2}$, $B_{c3}=E_{2\times2}$, k_{pPLL}, k_{iPLL}, k_{pc}, k_{ic} k_{pPQ}, k_{iPQ} and k_{pu}, k_{iu} represent the proportional and integral coefficients of the PLL unit, current control loop, power control loop and voltage control loop, respectively,

$$A_{PLL}=\begin{bmatrix} 0 & -U_{pccd0} & 0 \\ 0 & 0 & 1 \\ k_{iPLL}\omega_{MAF} & -k_{pPLL}U_{pccd0}\omega_{MAF} & -\omega_{MAF} \end{bmatrix} \tag{11}$$

$$B_{PLL}=\begin{bmatrix} 0 & 0 & 0 & 1 & 0 & 0 \\ 0 & 0 & 0 & 0 & 0 & 0 \\ 0 & 0 & 0 & k_{pPLL}\omega_{MAF} & 0 & 0 \end{bmatrix} \tag{12}$$

$$B_{cal}=\begin{bmatrix} 0\,0\ \frac{3}{2}\omega_c I_{gd0} & \frac{3}{2}\omega_c I_{gq0} & \frac{3}{2}\omega_c U_{pccd0} & \frac{3}{2}\omega_c U_{pccq0} \\ 0\,0-\frac{3}{2}\omega_c I_{gq0} & \frac{3}{2}\omega_c I_{gd0} & \frac{3}{2}\omega_c U_{pccq0} & -\frac{3}{2}\omega_c U_{pccd0} \end{bmatrix} \tag{13}$$

$$C_{PQ}=\begin{bmatrix} k_{iPQ} & 0 \\ 0 & -k_{iPQ} \end{bmatrix} \tag{14}$$

$$D_{PQ}=\begin{bmatrix} -k_{pPQ} & 0 \\ 0 & k_{pPQ} \end{bmatrix} \tag{15}$$

$$B_{c1} = \begin{bmatrix} 0 & -I_{q0} & 0 \\ 0 & I_{d0} & 0 \end{bmatrix} \tag{16}$$

$$B_{c2} = \begin{bmatrix} -1 & 0 & 0 & 0 & 0 & 0 \\ 0 & -1 & 0 & 0 & 0 & 0 \end{bmatrix} \tag{17}$$

$$D_{c2} = \begin{bmatrix} -k_{pc} - K_C & -\omega_g L_f & 1 & 0 & K_C & 0 \\ \omega_g L_f & -k_{pc} - K_C & 0 & 1 & 0 & K_C \end{bmatrix} \tag{18}$$

$$D_{c4} = \begin{bmatrix} 0 & -\left(K_C + k_{pc}\right) I_{q0} + \omega_g L_f I_{d0} + K_C I_{gq0} + U_{pccq0} - U_{q0} & 0 \\ 0 & \left(k_{pc} + K_C\right) I_{d0} + \omega_g L_f I_{q0} - K_C I_{gd0} - U_{pccd0} + U_{d0} & 0 \end{bmatrix} \tag{19}$$

$$A_{VSG} = \begin{bmatrix} -D/J & 0 & 0 \\ 1 & 0 & 0 \\ 0 & -k_q k_u U_{pccq0} & 0 \end{bmatrix} \tag{20}$$

$$B_{VSG1} = \begin{bmatrix} -1/J\omega_g & 0 \\ 0 & 0 \\ 0 & -k_q \end{bmatrix} \tag{21}$$

$$B_{VSG2} = \begin{bmatrix} 0 & 0 & 0 & 0 & 0 & 0 \\ 0 & 0 & 0 & 0 & 0 & 0 \\ 0 & 0 & -k_q k_u & 0 & 0 & 0 \end{bmatrix} \tag{22}$$

$$B_{u1} = \begin{bmatrix} 0 & -U_{pccq0} & 1 \\ 0 & U_{pccd0} & 0 \end{bmatrix} \tag{23}$$

$$B_{u2} = \begin{bmatrix} 0 & 0 & \text{-}1 & 0 & 0 & 0 \\ 0 & 0 & 0 & \text{-}1 & 0 & 0 \end{bmatrix} \tag{24}$$

$$D_{u1} = \begin{bmatrix} 0 & -k_{pu} U_{pccq0} + \omega_g C_f U_{pccd0} & k_{pu} \\ 0 & k_{pu} U_{pccd0} + \omega_g C_f U_{pccq0} & 0 \end{bmatrix} \tag{25}$$

$$D_{u2} = \begin{bmatrix} 0 & 0 & -k_{pu} & -\omega_g C_f & 0 & 0 \\ 0 & 0 & \omega_g C_f & -k_{pu} & 0 & 0 \end{bmatrix} \tag{26}$$

$$A_{LCL} = \begin{bmatrix} 0 & \omega & -1/L_f & 0 & 0 & 0 \\ -\omega & 0 & 0 & -1/L_f & 0 & 0 \\ 1/C_f & 0 & 0 & \omega & -1/C_f & 0 \\ 0 & 1/C_f & -\omega & 0 & 0 & -1/C_f \\ 0 & 0 & 1/L_g & 0 & -R_g/L_g & \omega \\ 0 & 0 & 0 & 1/L_g & -\omega & -R_g/L_g \end{bmatrix} \tag{27}$$

$$B_{LCL1} = \begin{bmatrix} 1/L_f & 0 & 0 & 0 & 0 & 0 \\ 0 & 1/L_f & 0 & 0 & 0 & 0 \end{bmatrix}^T \tag{28}$$

$$B_{LCL2} = \begin{bmatrix} 0 & 0 & 0 & 0 & -1/L_g & 0 \\ 0 & 0 & 0 & 0 & 0 & -1/L_g \end{bmatrix}^T \tag{29}$$

REFERENCES

[1] J. Rocabert, A. Luna, F. Blaabjerg, and P. Rodríguez, “Control of Power Converters in AC Microgrids,” *IEEE Trans. Power Electron.*, vol. 27, no. 11, pp. 4734-4749, Nov. 2012.

[2] X. Wang, M. G. Taul, H. Wu, Y. Liao, F. Blaabjerg, and L. Harnefors, “Grid-Synchronization Stability of Converter-Based Resources—An Overview,” *IEEE Open J. Ind. Appl.*, vol. 1, pp. 115-134, 2020.

[3] IEEE Guide for Planning DC Links Terminating at AC Locations Having Low Short-Circuit Capacities, IEEE Standard 1204-1997, NY, USA, 1997.

[4] C. Tu, J. Gao, F. Xiao, Q. Guo and F. Jiang, "Stability Analysis of the Grid-Connected Inverter Considering the Asymmetric Positive-Feedback Loops Introduced by the PLL in Weak Grids," *IEEE Trans. Ind. Electron.*, vol. 69, no. 6, pp. 5793-5802, June 2022.

[5] H. Gong, X. Wang and L. Harnefors, "Rethinking Current Controller Design for PLL-Synchronized VSCs in Weak Grids," *IEEE Trans. Power Electron.*, vol. 37, no. 2, pp. 1369-1381, Feb. 2022.

[6] R. Rosso, X. Wang, M. Liserre, X. Lu, and S. Engelken, “Grid-Forming Converters: Control Approaches, Grid-Synchronization, and Future Trends—A Review,” *IEEE Open J. Ind. Appl.*, vol. 2, pp. 93-109, 2021.

[7] L. Huang, C. Wu, D. Zhou and F. Blaabjerg, "A Double-PLLs-Based Impedance Reshaping Method for Extending Stability Range of Grid-Following Inverter Under Weak Grid," *IEEE Trans. Power Electron.*, vol. 37, no. 4, pp. 4091-4104.

[8] N. Pogaku, M. Prodanovic and T. C. Green, "Modeling, Analysis and Testing of Autonomous Operation of an Inverter-Based Microgrid," *IEEE Trans. Power Electron.*, vol. 22, no. 2, pp. 613-625, March 2007.

[9] J. Sun, "Impedance-Based Stability Criterion for Grid-Connected Inverters," *IEEE Trans. Power Electron.*, vol. 26, no. 11, pp. 3075-3078, Nov. 2011.

[10] X. Gao, D. Zhou, A. Anvari-Moghaddam and F. Blaabjerg, "Stability Analysis of Grid-Following and Grid-Forming Converters Based on State-Space Model," in *Proc. 10th Int. Conf. Power Electron. ECCE Asia*, Himeji, Japan, 2022, pp. 422-428.

[11] A. Sangwongwanich, A. Abdelhakim, Y. Yang, and K. Zhou, “Control of Single-Phase and Three-Phase DC/AC Converters,” in *Control of Power Electronic Converters and Systems*. F. Blaabjerg, Ed. Cambridge: Academic Press, 2018, pp. 153-173.

[12] D. Yang, and X. Wang, “Unified Modular State-Space Modeling of Grid-Connected Voltage-Source Converters,” *IEEE Trans. Power Electron.*, vol. 35, no. 9, pp. 9700-9715, Sept. 2020.

[13] D. Zhou, and F. Blaabjerg, “Bandwidth oriented proportional-integral controller design for back-to-back power converters in DFIG wind turbine system,” *IET Renewable Power Gener.*, vol. 11, no. 7, pp. 941-951, 2017.

[14] X. Wang, L. Harnefors, and F. Blaabjerg, “Unified impedance model of grid-connected voltage-source converters,” *IEEE Trans. Power Electron.*, vol. 33, no. 2, pp. 1775-1787, Feb. 2017.

[15] S. Golestan, M. Ramezani, J. M. Guerrero, F. D. Freijedo and M. Monfared, "Moving Average Filter Based Phase-Locked Loops: Performance Analysis and Design Guidelines," *IEEE Trans. Power Electron.*, vol. 29, no. 6, pp. 2750-2763, June 2014.

[16] L. Yang *et al.*, “Effect of phase-locked loop on small-signal perturbation modelling and stability analysis for three-phase LCL-type inverter connected to weak grid,” *IET Renewable Power Gener.*, vol. 13, no. 1, pp. 86-93, 2019.

[17] D. Dong, B. Wen, D. Borowiecki, P. Mattavelli, and Y. Xue, “Analysis of Phase-Locked Loop Low-Frequency Stability in Three-Phase Grid-Connected Power Converters Considering Impedance Interactions,” *IEEE Trans. Ind. Electron.*, vol. 62, no. 1, pp. 310-321, Jan. 2015.

[18] Z. Xie *et al*., “Modeling and control parameters design for grid-connected inverter system considering the effect of PLL and grid impedance,” *IEEE Access*, vol. 8, pp. 40474-40484, 2019.

[19] B. Wen, D. Boroyevich, R. Burgos, P. Mattavelli, and Z. Shen, “Analysis of D-Q Small-Signal Impedance of Grid-Tied Inverters,” *IEEE Trans. Power Electron.*, vol. 31, no. 1, pp. 675-687, Jan. 2016.

[20] A. K. Adapa, and V. John, “Virtual resistor based active damping of LC filter in standalone voltage source inverter,” in *Proc. IEEE Appl. Power Electron. Conf. Expo. APEC*, San Antonio, TX, USA, 2018, pp. 1834-1840.

[21] P. A. Dahono, Y. R. Bahar, Y. Sato, and T. Kataoka, “Damping of transient oscillations on the output LC filter of PWM inverters by using a virtual resistor,” in *Proc. 4th IEEE Int. Conf. Power Electron. Drive Sys.*, Denpasar, Indonesia, 2001, pp. 403-407.

[22] W. Wu *et al.*, “Sequence-Impedance-Based Stability Comparison Between VSGs and Traditional Grid-Connected Inverters,” *IEEE Trans. Power Electron.*, vol. 34, no. 1, pp. 46-52, Jan. 2019.

[23] J. A. Suul, S. D'Arco, P. Rodríguez, and M. Molinas, “Impedance-compensated grid synchronisation for extending the stability range of weak grids with voltage source converters,” *IET Gener. Transm. & Distrib.*, vol. 10, no. 6, pp. 1315-1326, 2016.

[24] M. Wang *et al.*, "Review and outlook of HVDC grids as backbone of transmission system", *CSEE Journal of Power and Energy Systems*, vol.7, no.4, pp.797-810, 2021.

[25] Spitzenberger & Spies, 2021. “SPS-TD-APS-Overview-1107-e-0008,” https://spitzenberger.de/weblink/1107.

[26] Imperix, Mar. 2021, “PEB8024 - Half-bridge SiC power module,” https://cdn.imperix.com/wp-content/uploads/document/PEB8024.pdf?_gl=1*1imyt74*_ga*OTM5NTQ5MzAwLjE2NzI4NjQxMDc.*_ga_B703CE28ZY*MTY3Mjg2NDEwNi4xLjEuMTY3Mjg2NDU0My4wLjAuMA..&_ga=2.13694581.315351586.1672864107-939549300.1672864107.

[27] C. Li, J. Liang, L. M. Cipcigan, W. Ming, F. Colas and X. Guillaud, "DQ Impedance Stability Analysis for the Power-Controlled Grid-Connected Inverter," *IEEE Trans. Energy Convers.*, vol. 35, no. 4, pp. 1762-1771, Dec. 2020.

[28] X. Gao, D. Zhou, A. Anvari-Moghaddam and F. Blaabjerg, "Analysis of X/R Ratio Effect on Stability of Grid-Following and Grid-Forming Converters," in *Proc. 17th Int. Conf. Compat., Power Electron. Power Eng. CPE-POWERENG*, Tallinn, Estonia, 2023, pp. 1-6.